Nd and Ni Co-doped spinel Co_3O_4 nanosheet as an effective electrocatalyst for oxygen evolution reaction

Tao Li [a], Zhijin Wang [a], Linhai Wang [a], Mingyu Wang [b], Yun-Quan Liu [a,b,*]

[a] College of Energy, Xiamen University, Xiamen 361102, China
[b] Shengyuan (Xiamen) Hydrogen Energy Research Institute, Xiamen 361013, China

ARTICLE INFO

ABSTRACT

It is well known that the regulation of active sites in tetrahedrons (Td) and octahedrons (Oh) can improve the electrocatalytic performance of the spinel oxides (AB_2O_4) type materials when used for oxygen evolution reaction (OER). However, the effect of site modulation on the surface reconstruction in electrocatalyst is still not clear during the OER process. In this work, NdNi-Co_3O_4 was prepared by introducing Ni^{2+} and Nd^{3+} into Co_3O_4, which exhibited an excellent activity with an overpotential of 269 mV at 10 mA·cm^{-2} and a Tafel slope of 54 mV·dec^{-1}. In-situ Raman spectroscopy showed that the catalyst surface apparently underwent a reconstruction process with the generation of cobalt hydroxyl oxides (CoOOH) after Ni-substitution, and the further introduction of Nd led to the formation of CoOOH at lower potential. DFT calculations revealed that the introduction of Ni and Nd not only modulated the electronic structure of the reconstructed catalyst and the appropriate interactions for the intermediates, but also changed its potential determining step (PDS) from the O_2 generation to the generation of hydroxyl oxides (i.e. O*→OOH*), which effectively reduced the energy barrier for OOH* generation, thus resulting in excellent OER performance.

1. Introduction

The growing global energy demand and worsening environment have attracted a lot of interest in developing sustainable energy storage and conversion technologies, such as metal-air batteries and water splitting materials for hydrogen production [1,2]. The oxygen evolution reaction (OER), an important half-reaction often encountered in energy conversion technologies, usually determines the electrochemical performance and stability of catalysts [3,4]. Although Ru and Ir-based materials are the most efficient and the state-of-the-art OER electrocatalysts, large scale applications of them are still very limited to date because of their high prices [5,6]. Therefore, non-noble metal based OER catalysts that have excellent activity and durability are imperative to be developed [7].

The spinel oxides (AB_2O_4), consisting of a tetrahedral coordination of A^{2+} (A_{Td}^{2+}) and an octahedral coordination of B^{3+} (B_{Oh}^{3+}), had showed improved electrocatalytic activity and stability for OER in alkaline electrolytes [8–11]. For example, Shao et al. demonstrated that the redox capability of lattice oxygen can be activated by introducing F ions into the oxygen vacancies of spinel $ZnCo_2O_4$, which promoted the OER activity [12]. It is also generally accepted that the spinel oxides are

pre-catalysts for OER, and their surfaces will be significantly reconstructed into hydroxyl oxide (MOOH) species in alkaline conditions during the OER process [13,14]. It has been reported that the chemical reconstruction on the surface of $MnCo_2O_4$ can be achieved by applying ZIF-derived $MnCo_2O_4$/CeO_2 heterostructures to OER [15]. In addition, Shao et al. enabled $Li_2Co_2O_4$ to generate a controlled and layered $LiCoO_2$ phase and spinel Co_3O_4 by adjusting the pyrolysis temperature, in which Co_3O_4 was transformed into the active species like $CoOOH_x$ during the OER process [16]. Besides being able to construct heterostructures, the transition metal-doping is also an important method for facilitating the surface reconstruction of spinel oxides [17]. For example, the surface reconstruction of Ni-Co_3O_4 was facilitated by iron doping, which could accelerate the formation of the active species of NiOOH and improve the water oxidation activity of catalysts [18]. Depending on their electronic configuration and valence state, other transition metal cations can also be used for substituting the active sites in tetrahedral and octahedral, respectively, both of which affect the distribution of the defects in spinel oxides as well as the electronic structure of the active metal sites. However, the effectiveness varies from site to site [19,20]. Several previous works have proposed that the OER performance of spinel oxides were related to the Td site. Wu et al.

---

prepared a series of spinel oxides ACo_2O_4 (A = Mn, Co, Ni, Cu, Zn) by substituting the A site with different transition metals, which led to a shift in the d-band center along with modulation of the Co^{3+}/Co^{2+} ratio, demonstrating that A site plays an important role in enhancing the OER performance of spinel [21]. Liu et al. found that the A_{Td}^{2+} and B_{Oh}^{3+} sites of Co_3O_4 were replaced by the inactive Zn^{2+} and Al^{3+}, respectively, where A_{Td}^{2+} determines the formation of cobalt hydroxide (CoOOH), which is the active site for water oxidation [22]. It was also found that the Co doping in octahedral $ZnCo_xMn_{2-x}O_4$ enables the rate-limiting step of OER [23]. In general, both 4 f-rare-earth metals and 3d-transition metals can be used to form spinel-type oxides that exhibit a similar effect in enhancing OER activity, for example, increasing the vacancy concentration, enhancing the intrinsic catalytic activity, and accelerating the dynamic reconstruction of the active phase during the OER process [24]. Moreover, the unfilled 4 f orbitals in 4 f-rare-earth metals would contribute to the optimization of local electronic state compared to the 3d-transition metals, which facilitates the enhancement of intrinsic electrocatalytic activity [25]. For example, Ce doped Co_3O_4 ($Ce-Co_3O_4$) would increase conductivity and modulate the ratio of Co^{3+}/Co^{2+} to enhance the adsorption/desorption of intermediates on Co_{oh}^{3+} for OER electrocatalysis [26].

In order to enhance the OER stability in alkaline conditions, on the other hand, rare-earth elements with oversized atomic radius and better stability can be introduced into the lattice of Co_3O_4 through partial doping, which will benefit to the generation of oxygen vacancies (V_O) and the improvement of corrosion resistance. In addition, the third transition metal with the similar size and charge to cobalt can be doped in the lattice of oxides for improving the catalytic activity. Based on the above thinkings, we prepared a Nd and Ni co-doped spinel Co_3O_4 through a simple ion substitution strategy to further extend from oxygen evolution reaction in three-electrode system to zinc-air battery or water-splitting in two-electrode system. For determining the real active sites of the catalysts during OER, the OER process was monitored in real time with an *in-situ* Raman. The results revealed that the introduction of Nd and Ni could indeed promote the surface reconstruction of spinel, and the modification of Td and Oh sites had different effects on the dynamic reconstruction of reactive metals like Co.

2. Experimental section

2.1. Synthesis of NdNi-Co₃O₄

In a typical preparing process of $NdNi-Co_3O_4$,1 mmol of Ni $(NO_3)_2 \cdot 6 H_2O$, 1.7 mmol of $Co(NO_3)_2 \cdot 6 H_2O$ and 0.3 mmol Nd $(NO_3)_3 \cdot 6 H_2O$ were dissolved in 25 ml of water under stirring. Next, 2 mmol urea and 5 mmol NH_4F were dissolved in 25 ml of water with agitation. The two solutions were mixed and sonicated for 30 min. Later, the mixed solution was transferred to a 100 ml Teflon-lined stainless-steel autoclave, which was then sealed and heated in an electric oven to 140°C, and maintained at this temperature for 7 h. The vessel was then naturally cooled to room temperature. The obtained precipitate was collected, washed with the distilled water and ethanol for several times, which was finally dried at 60°C for 12 h. The dried powder was then ground and calcined at 400°C for 2 hours in air atmosphere, so that a composite of Nd and Ni Co-doped Co_3O_4 was obtained, which was denoted as $NdNi-Co_3O_4$-2 in this work. When the amount of Nd was 0.2 and 0.4 mol, the obtained samples were named as $NdNi-Co_3O_4$-1 and $NdNi-Co_3O_4$-3, respectively.

2.2. Synthesis of Co₃O₄ and Ni-Co₃O₄

For the synthesis of Co_3O_4 or $Ni-Co_3O_4$, the similar procedures and conditions were followed, except that 3 mmol of $Co(NO_3)_2 \cdot 6 H_2O$ or 1 mmol of $Ni(NO_3)_2 \cdot 6 H_2O$ with 2 mmol of $Co(NO_3)_2 \cdot 6 H_2O$ were added, respectively.

3. Results and discussion

3.1. Characterization

The formation energies of Nd atoms located in tetrahedral and octahedral sites were calculated through the density functional theory (DFT), and the results are shown in Fig. 1a-b. As seen, Nd atoms are more stable when located at the Oh site (-4.2 eV) than located at the Td site (-3.6 eV) in spinel $Ni-Co_3O_4$. As also shown in the X-ray diffraction (XRD) pattern of Fig. 1c, the sharp characteristic peaks located at 2θ = 18.9, 31.1, 36.7, 38.4, 44.6, 55.4, 59.1 and 64.9° can be assigned to the cubic spinel phases (111), (311), (222), (400), (422), (511) and (440) for Co_3O_4 (JCPDS No.71–0816) [27,28]. Also, in Fig. 1d, four peaks (E_g, F_{2g}, F_{2g}, and A_{1g}) are clearly shown in the Raman pattern, where the $A_{1\,g}$ peak of $Ni-Co_3O_4$ and all the $NdNi-Co_3O_4$ showed a significant red shift due to increased vacancies in the spinel oxide which were caused by the introduction of Ni and Nd into Co_3O_4 [29]. Fig. 2a shows that $NdNi-Co_3O_4$ mainly exhibits a uniform nanosheet morphology, and from the enlarged SEM image in Fig. 2b we can see that the catalyst surface is composed of many nanoparticles, which might be beneficial to providing more active sites for the electrocatalytic process. The nanosheet structure of the catalyst was further evidenced by the TEM image in Fig. 2c. As seen, the HRTEM image shows lattice stripes with a lattice spacing of 0.245 nm, which can be attributed to the (311) plane of $NdNi-Co_3O_4$, indicating that the $NdNi-Co_3O_4$-2 surface was dominated by the (111) plane, and this is in agreement with the XRD results. As shown in Fig. 2e, the bright spots in the selected area electron diffraction (SAED) pattern are further indexed to the (111), (311), (222), and (400) planes of $Ni-Co_3O_4$. Fig. 2 f shows a scanning TEM (STEM) image of a typical sample with Ni, Co, Nd and O elements well dispersed; while Fig. 2 g with low content of Nd and O. The content of metal elements (including Ni, Co, Nd) in $Ni-Co_3O_4$ spinel oxide was measured using the inductively coupled plasma optical emission spectrometer (ICP-OES). As observed, with the increased Nd content in $NiCo_{2-x}Nd_xO_4$, the atomic ratio of Ni to the sum of Co and Nd can be determined, which is in the range of 1:1.85–1:1.89, and this value is very close to the theoretical ratio of Ni to Co in the $Ni-Co_3O_4$ sample, thus providing solid evidence that Co was partially substituted by Nd.

In order to understand the valence state of each element on catalyst surface, XPS spectrum were performed on these five spinel oxides, including Co_3O_4, $Ni-Co_3O_4$, $NdNi-Co_3O_4$-1, $NdNi-Co_3O_4$-2 and $NdNi-Co_3O_4$-3. The results indicated that the surface of catalyst contains four elements of Ni, Co, Nd, O (Figure S1). Additionally, as shown in Fig. 3a, the Ni 2p XPS of $NdNi-Co_3O_4$-2 had peaks at 853.7/871.5 and 855.6/873.2 eV, indicating the +2 and +3 oxidation states of Ni species, respectively [30]. Moreover, as shown in Fig. 3b, two fitted peaks at 779.5 and 794.8 eV for $NdNi-Co_3O_4$-2 were observed, which are corresponding to Co^{3+} $2p_{3/2}$ and Co^{3+} $2p_{1/2}$, respectively. The other two peaks at 781.2 and 796.7 eV are corresponding to Co^{2+} $2p_{1/2}$ and Co^{2+} $2p_{3/2}$ [31]. In Fig. 3c, the O 1 s can be fitted with the three peaks at 529.4, 531.3 and 532.9 eV. Specifically, the peak at 529.4 eV was for the lattice oxygen (O_L), while the peak at 531.3 eV for the oxygen vacancy (O_V), and the peak at 532.9 eV for water molecules and hydroxyl groups adsorbed on the catalysts surface [32]. Finally, the peaks at 973.5 eV and 993.0 eV are ascribed to Nd^{3+} $3d_{5/2}$ and Nd^{3+} $3d_{3/2}$ in Nd 3d spectra (Fig. 3d), respectively [33]. According to the Co 2p XPS spectra given in Fig. 3b, the Co $2p_{1/2}$ and Co $2p_{3/2}$ peaks of $Ni-Co_3O_4$ and $NdNi-Co_3O_4$-2 were shifted toward the lower binding energy region compared to Co_3O_4, indicating the existence of electron coupling and electron transfer between Ni_{Td}^{2+} and Co_{Oh}^{3+}. This negative shift was greatly contributed to the optimal regulation of electronic structures and the further improved reaction rate of the interfacial catalytic process [34]. In addition, most of cobalt cations in the $NdNi-Co_3O_4$-2 sample are in the form of Co^{2+}. Compared to the other four samples, $NdNi-Co_3O_4$-2 presented higher peaks associated with Co^{2+} ions, which were identified as the active sites for OER, and its Co^{2+}/Co^{3+} ratio is 1.6 times that of
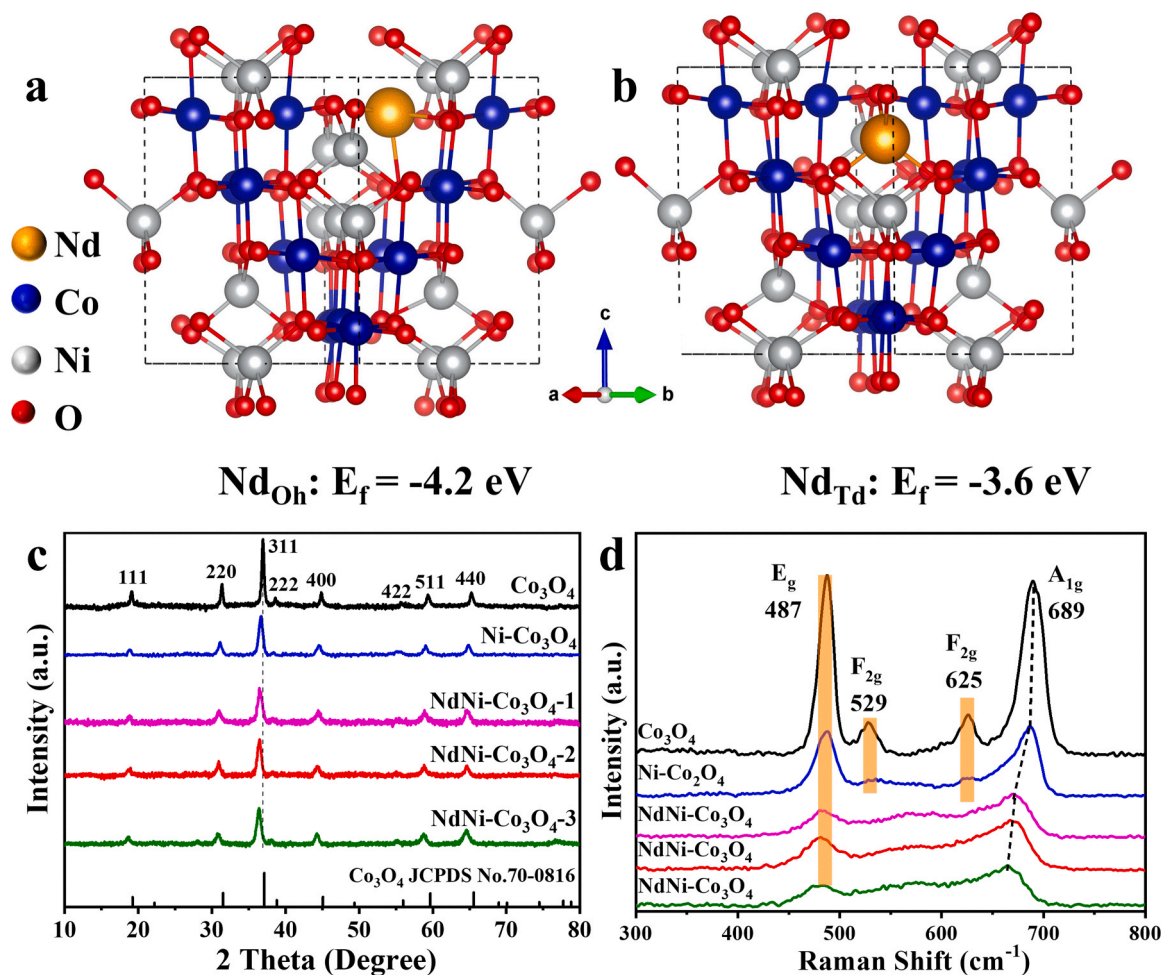
Fig. 1. Structural diagram of Nd and Ni co-doped Co_3O_4: (a) Nd^{3+} occupies the Oh site; (b) Nd^{3+} occupies the Td site. (c) XRD patterns and (d) Raman Spectrum of the catalysts.

Co_3O_4 [35,36]. While in Ni 2p, the relative contents of Ni^{3+} and Ni^{2+} were almost no changed before and after the introduction of Nd, indicating that the introduction of Nd had almost no effect on the valence state of Ni. In O 1 s, however, the binding energy of O_L was significantly and negatively shifted (1.0 V) after the introduction of Ni, with the content of O_V increased by ~15%; while the binding energy of $O_{L,}$ after the introduction of Nd, was slightly and negatively shifted (0.1 V), with the content of O_V continued to increase to ~20% [37]. It was shown that the introduction of both Nd and Ni led to a significant increase in defects in the catalyst, which is consistent with our intention for the design of catalysts.

3.2. Electrocatalytic measurements

The effect of Nd and Ni co-doping on the OER/ORR electrocatalytic activities of $NdNi-Co_3O_4$ was investigated. Figure S3 is the redox peak of $NdNi-Co_3O_4$-2, corresponding to the conversion of Co^{2+} into higher oxidation state $Co^{3+/4+}$ species, which was observed at lower potentials for $NdNi-Co_3O_4$-2 than for Co_3O_4 or $Ni-Co_3O_4$ [38]. The linear sweep voltammetry (LSV) curves and the corresponding Tafel slopes of Co_3O_4, $Ni-Co_3O_4$, $NdNi-Co_3O_4$-1, $NdNi-Co_3O_4$-2 and $NdNi-Co_3O_4$-3 were measured in 1 M KOH solution, which were then compared with the commercial RuO_2 catalyst shown in Fig. (3a, b). As seen, at 10 mA·cm^{-2} and 50 mA·cm^{-2}, the overpotential of $NdNi-Co_3O_4$ was 269 mV and 310 mV, respectively, which is significantly lower than that of Co_3O_4 (393 mV and 509 mV) and of $Ni-Co_3O_4$ (305 mV and 362 mV) (see Fig. 3a, c). In addition, when the content of Nd was 0.2 or 0.4, the

overpotential at 10 mA·cm^{-2} was 360 or 311 mV, respectively. At the same time, the overpotential of RuO_2 was only 292 mV at 10 mA·cm^{-2}. The reaction kinetics for the developed catalysts during the OER process was evaluated with the Tafel slope (Fig. 3b). As seen, the Tafel slope of $NdNi-Co_3O_4$ (54 mV·dec^{-1}) was smaller than that of Co_3O_4 (70 mV·dec^{-1}) and of $Ni-Co_3O_4$ (63 mV·dec^{-1}), indicating a faster catalytic kinetics of $NdNi-Co_3O_4$ compared to the other two catalysts in alkaline media (Fig. 3c). The activity of the catalysts obtained through oxidation at different temperatures from 300°C to 600°C was also evaluated (Figure S4a-e). The results showed that the catalyst $NdNi-Co_3O_4$, which maintains a nanosheet structure, exhibited the best activity corresponding to an oxidation temperature of 400°C (Figure S5a-c) [39].

The double layer capacitance (C_{dl}) was evaluated with the CV in the non-Faraday range (Figure S6). Also, the electrocatalytically active surface area (ECSA) was estimated for better understanding the intrinsic activity of the catalyst (see the inset of Fig. 4d) [40]. In Fig. 4d, the current density of $NdNi-Co_3O_4$-2 (0.0089 mA·cm$_{ECSA}^{-2}$) at 1.53 V is nearly 4.0 times of that of Co_3O_4 (0.0022 mA·cm$_{ECSA}^{-2}$) and of $Ni-Co_3O_4$ (0.0025 mA·cm$_{ECSA}^{-2}$), it means that $NdNi-Co_3O_4$ had higher intrinsic activity than Co_3O_4 and $Ni-Co_3O_4$. To further analyze the OER intrinsic activity of these catalysts, the turnover frequency (TOF) for each surface site was determined [41]. The calculated TOFs versus the potential are displayed in Figure S7. As seen, at 300 mV vs RHE, the TOF for $NdNi-Co_3O_4$, $Ni-Co_3O_4$ and Co_3O_4 was 3.43, 0.66, and 0.058 s^{-1}, respectively. And the same sequence was observed at higher potentials, which confirms that the OER intrinsic activity of the spinel oxide $NdNi-Co_3O_4$ was
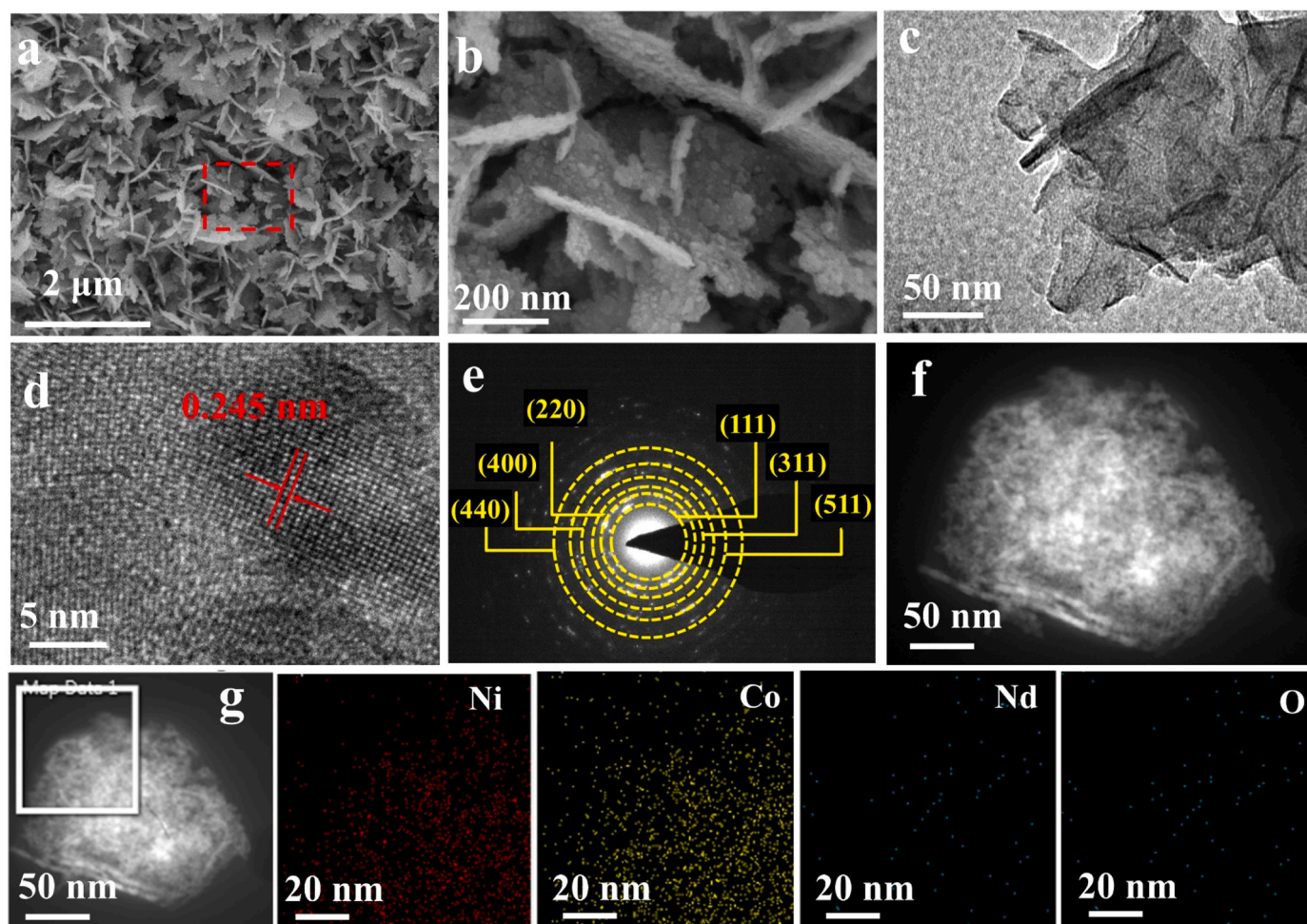
Fig. 2. (a, b) SEM, (c) Low-magnification TEM, (d) HRTEM images (e) SAED pattern and (f) HAADF-STEM image and (g) EDS mappings of NdNi-Co$_3$O$_4$-2.

much higher than that of Ni-Co$_3$O$_4$ and Co$_3$O$_4$. As an OER catalyst with higher activity in alkaline media, NdNi-Co$_3$O$_4$ showed a better performance compared to the other spinel-type metal oxides found in literature (Figure S8). The durability of NdNi-Co$_3$O$_4$ was analyzed through chronopotentiometry at the potentials of 1.50 and 1.54 V (Fig. 4e). As seen, the overpotential was increased by only 12 mV and 28 mV after 50 h, respectively, which were much better than that of RuO$_2$ (Figure S8b). This means that NdNi-Co$_3$O$_4$ had the best OER durability at alkaline conditions, especially at higher current densities [18].

The charge transfer kinetics of Co$_3$O$_4$, Ni-Co$_3$O$_4$, NdNi-Co$_3$O$_4$ in OER processes was further investigated through electrochemical impedance spectroscopy (EIS), which is a potential dependent method. The Nyquist plots and the corresponding Bode plots for Co$_3$O$_4$, Ni-Co$_3$O$_4$ and NdNi-Co$_3$O$_4$ are shown in Fig. 5a-c and Figure S9a-c, respectively. Since the impedance spectra in Fig. 5a-c showed a severe overlap at low potentials, in order to obtain more accurate analytical results, the distribution of relaxation times (DRT) method was used to analyze the variation of the different resistances during OER. Additionally, in Figure S9d-f, the resistance consists mainly of three parts, labelled P$_1$, P$_2$ and P$_3$. The R$_s$ part is for solution resistance, the R$_{eo}$ is for electrooxidation resistance; and the R$_{ct}$ part is for charge transfer resistance (R$_{ct}$) [42,43]. Peak areas of P$_1$, P$_2$ and P$_3$ represent the corresponding values of R$_s$, R$_{eo}$ and R$_{ct}$ of the three catalysts, which are summarized in Fig. 5d-f. It can be clearly seen that the R$_{eo}$ of NdNi-Co$_3$O$_4$ was much lower than that of Co$_3$O$_4$ and Ni-Co$_3$O$_4$ before the OER, as the Co^{2+} content in NdNi-Co$_3$O$_4$ is lower than in others. As further observed, when the potential applied to the working electrode begins to increase, the R$_{eo}$ and the phase angle in HF region became smaller for all three catalysts, indicating that the

resistance for catalysts electrooxidation begins to decrease. When the applied potential reached 1.274 V, the R$_{eo}$ of Co$_3$O$_4$ decreased at a slower rate (Fig. 5d). In comparison, the R$_{eo}$ of Ni-Co$_3$O$_4$ and NdNi-Co$_3$O$_4$ decreased at an accelerated rate (Fig. 5e, f), indicating that the surface reconstruction most likely happened in catalysts, thus resulting in the accelerated electrooxidation process [44]. The decreasing trend of NdNi-Co$_3$O$_4$ is more distinct than that of Ni-Co$_3$O$_4$, signaling that the Nd substitution of Co had a positive effect on surface reconstruction [45]. Moreover, the R$_{ct}$ of NdNi-Co$_3$O$_4$ was significantly lower than that of Co$_3$O$_4$ and Ni-Co$_3$O$_4$ at the 1.524 V (inset of Fig. 5d-f), illustrating that NdNi-Co$_3$O$_4$ exhibited faster electrocatalytic reaction kinetics than other catalysts [46]. In summary, the introduction of both Ni and Nd into Co$_3$O$_4$ is effective in decreasing the resistance in electrooxidation, as the co-doping of Ni and Nd would contribute to faster interfacial charge transfer and transport of intermediates, thus accelerating surface reconstruction of catalysts during the OER process [47].

On the other hand, its ORR activity was also slightly improved after the introduction of Ni and Nd, as the electronic structure of NdNi-Co$_3$O$_4$ nanosheet was also improved [48]. Shown in Fig. 4f is the LSV of the catalyst measured in 0.1 M KOH, which was compared to the commercial 20% Pt/C catalyst. As observed, NdNi-Co$_3$O$_4$ showed a better ORR performance (limiting current density J$_L$ = 5.89 mA·cm^{-2} and half-wave potential E$_{1/2}$ = 0.764 V) than Co$_3$O$_4$ (4.68 mA·cm^{-2}, 0.701 V), Ni-Co$_3$O$_4$ (4.49 mA·cm^{-2}, 0.761 V), NdNi-Co$_3$O$_4$-1 (5.04 mA·cm^{-2}, 0.754 V) and NdNi-Co$_3$O$_4$-3 (5.43 mA·cm^{-2}, 0.747 V) [49]. The long-term stability of NdNi-Co$_3$O$_4$ and Pt/C was measured using the chronoamperometry. As shown in Figure S10, NdNi-Co$_3$O$_4$-2 exhibited a better stability with a slight current loss of 5% after 20 h operation at
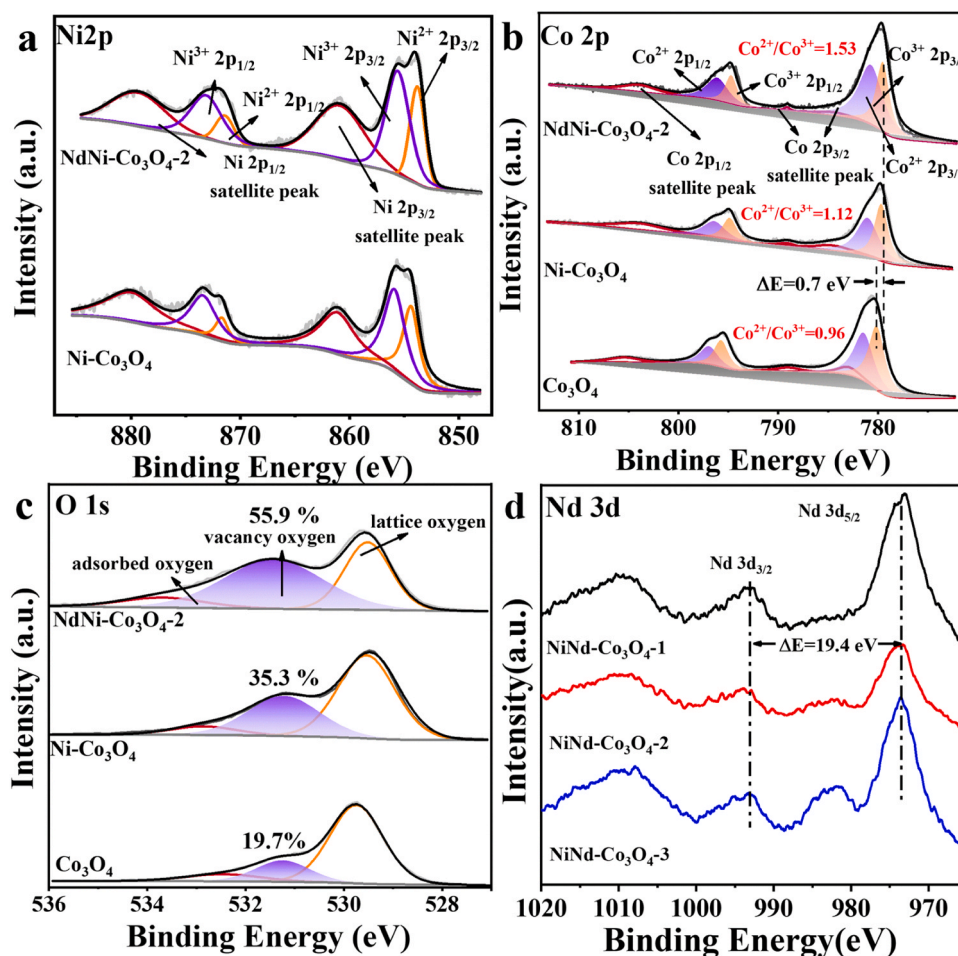
Fig. 3. XPS spectra of (a)Ni 2p, (b)Co 2p, (c) O 1 s and (d) Nd 3d of the catalysts.

0.4 V, much lower than that of Pt/C. Furthermore, the bifunctional electrocatalytic activity for all the prepared catalysts was compared. As seen, the difference between $E_{1/2}$ for ORR and the overpotential at $E_{j=10}$ for OER ($\triangle E = E_{1/2}\text{-}E_{j=10}$) was ranked in the following order: NdNi-Co$_3$O$_4$-2 (0.735 V) < Ni-Co$_3$O$_4$ (0.774 V) < NdNi-Co$_3$O$_4$-3 (0.794 V) < NdNi-Co$_3$O$_4$-1 (0.836 V) < Co$_3$O$_4$ (0.922 V), demonstrating that Ni and Nd could enhance the bifunctional performance of NdNi-Co$_3$O$_4$ (Fig. 4g and Figure S11) [50]. Additionally, the bifunctional performance of NdNi-Co$_3$O$_4$ was evaluated in a rechargeable Zn-Air battery. As observed, NdNi-Co$_3$O$_4$ catalyst exhibited a better battery performance than Pt/C+RuO$_2$ (Figure S12) [51].

Like Ni doped Co$_3$O$_4$, the Co-based spinel oxides, such as Mn doped Co$_3$O$_4$ and Fe doped Co$_3$O$_4$, have also been reported efficient electrocatalysts for OER [52,53]. Therefore, NdMn-Co$_3$O$_4$ and NdFe-Co$_3$O$_4$ were prepared through a similar method. The samples were identified by SEM (Figure S13a-b), and the morphology of the samples was found to be nanorod-based dendritic and urchin-like structure for NdMn-Co$_3$O$_4$ and NdFe-Co$_3$O$_4$. The XRD spectra of the samples were in good agreement with the standard cards (Figure S13c) [52,53]. The elemental composition and electronic state of the samples were further characterized using XPS (Figure S14,15). As indicated, the successful synthesis of the desired spinel oxides was achieved. The OER performance of NdMn-Co$_3$O$_4$, NdFe-Co$_3$O$_4$ and Co$_3$O$_4$ was also measured in a 1 M KOH solution. As shown in Figure S16a-c, the overpotentials of NdMn-Co$_3$O$_4$ and NdFe-Co$_3$O$_4$ were decreased by 42 mV and 97 mV, respectively, in comparison with Co$_3$O$_4$, illustrating the importance of Fe (Mn) and Nd doping in the enhancement of Co$_3$O$_4$ activity. The measured results of Tafel plots were consistent with LSV. In addition, the C_{dl} value of

NdFe-Co$_3$O$_4$ was 1.96 mF·cm^{-2} (Figure S17), 2.5 times that of Co$_3$O$_4$. From the above results, it can be derived that the co-doping of Co$_3$O$_4$ with Ni (Fe, Mn) and Nd played an identical role in increasing the content of vacancies and in improving the electronic structure of Co, which in turn had a positive effect on the OER activity of catalysts. Moreover, other rare-earth metals such as lanthanum (La), cerium (Ce), praseodymium (Pr), samarium (Sm) and europium (Eu) were also investigated, which were shown in Figure S18. As seen, most of rare-earth metal doped catalysts exhibited better OER activities than Co$_3$O$_4$. And the overpotentials of both rare earth metal and Ni co-doped Co$_3$O$_4$ catalysts were found increasing first and then decreasing, which could be attributed to the fact that the OER activity of catalysts may be highly dependent on the atomic radius of the doped rare earth metals. That is, the OER activity would increase initially and then decrease with the decreasing in average atomic radius [54–56].

3.3. Insights into the Mechanism of OER

Raman spectra were recorded through increasing the potential at the interval of 0.05 V, and our goal is to further reveal the effect of the co-doping of Ni and Nd into spinel catalysts on OER performance (Fig. 6a-c). As seen in Fig. 6a, four Raman peaks, located at 489, 529, 626 and 696 cm^{-1}, corresponding to E_g, $F_{2g(1)}$, $F_{2g(2)}$ and A_{1g}, respectively, were seen, which are similar to that of Co$_3$O$_4$ before the OER [57]. In comparison with Co$_3$O$_4$, however, there are only three peaks in Ni-Co$_3$O$_4$ (Fig. 6b), a peak at 485 cm^{-1}, which may be attributed to the vibration of Co-O in the Ni-Co$_3$O$_4$ crystal), a peak at 574 cm^{-1} which may be assigned to the Co-O in defective or in disordered Ni-Co$_3$O$_4$, and a third
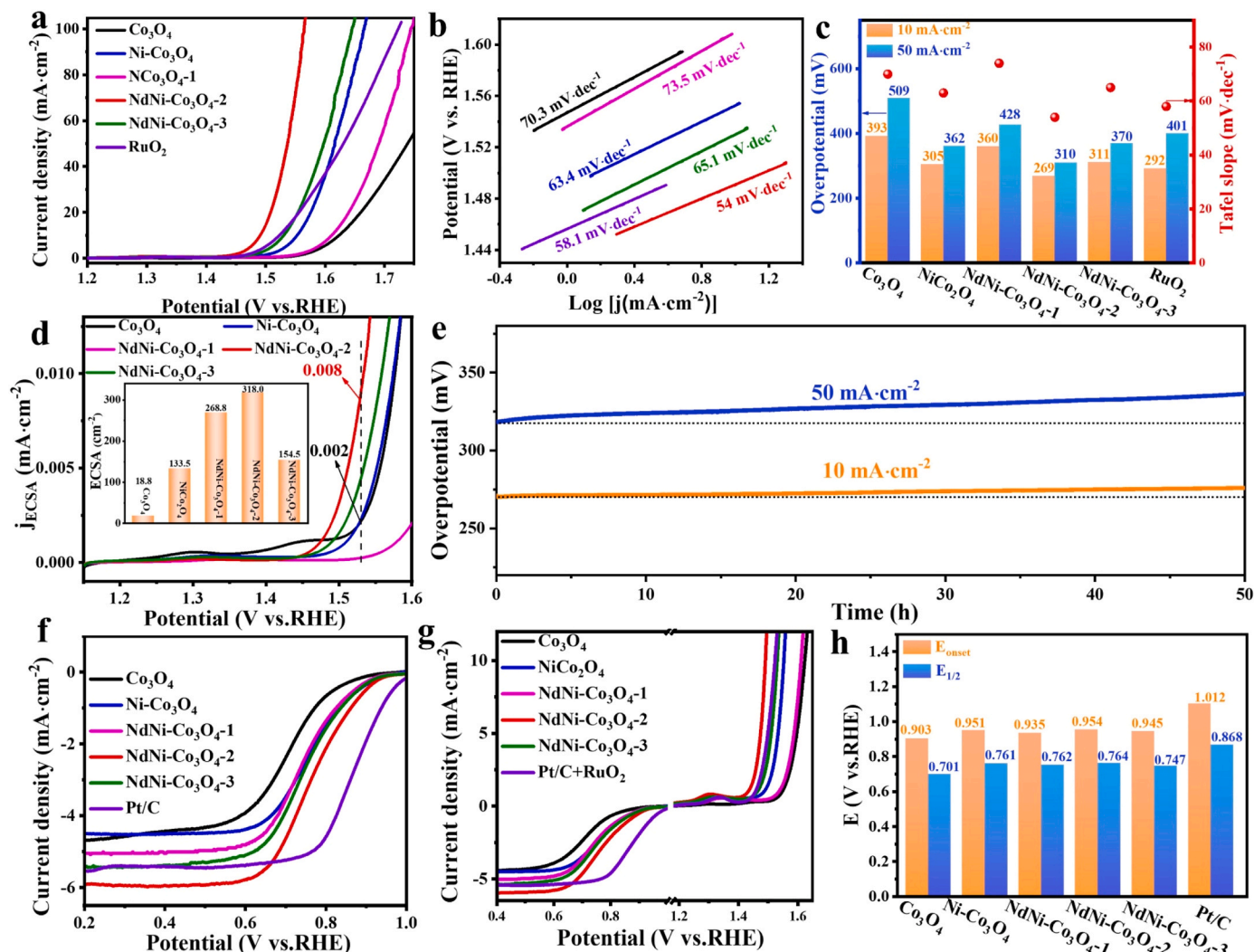
Fig. 4. (a) Polarization curves of the catalysts in1 M KOH at a scan rate of 5 mV·s^{-1}. (b) Tafel plots of the catalysts derived from Fig. 4a. (c) Comparison of overpotential at 10 mA·cm^{-2} and 50 mA·cm^{-2} and Tafel slope for OER activity. (d) ECSA corrected LSV of the electrocatalysts (the ECSA value of the electrocatalysts). (e) Chronopotentiometry tests of NdNi-Co$_3$O$_4$-2 at 10 mA·cm^{-2} and 50 mA·cm^{-2}. (f) LSV polarization curves of the catalysts in 0.1 M KOH at a scan rate of 10 mV·s^{-1}. (g) Entire LSV curve of bifunctional activity of ORR and OER, (h) Comparison of E$_{onset}$ and E$_{1/2}$ for ORR activity.

peak at 696 cm^{-1}, which might be attributed to the O-M-O mode of Ni-Co$_3$O$_4$ [58]. When the potential applied to the working electrode was increased, the four peaks attributed to Co$_3$O$_4$ were stable, that is, no shifts or new peaks appeared, indicating that the Co$_3$O$_4$ had not reconstructed during the OER process [26]. For Ni-Co$_3$O$_4$, the peak at 574 cm^{-1} had only small change (decrease first and then increase) with the increased potential, suggesting that the localized disorder of Co-O in Ni-Co$_3$O$_4$ is almost invariant (Fig. 6d). In contrast, the peak at 572 cm^{-1} of NdNi-Co$_3$O$_4$ increased rapidly with the increased potential, indicating that an increase in the localized disordered of Co-O, and the start of the transformation of cobalt oxide from crystalline to amorphous gradually (Fig. 6d). A new and weak peak at 561 cm^{-1} appeared when the potential was increased to 1.374 V, which is attributed to the transformation from amorphous cobalt oxide to amorphous CoOOH [18]. The peak's intensity of $\delta_{(Co-O)}$ and $\nu_{(Co-O)}$ in CoOOH continued increase from 1.374 V to 1.524 V, indicating the content of CoOOH in the catalyst increased and the reconstruction deepened [59]. More notably, cobalt hydroxides were generated in Ni-Co$_3$O$_4$ at only 1.424 V, while the surface reconstruction of Ni-Co$_3$O$_4$ started at a higher potential than NdNi-Co$_3$O$_4$. The above results indicated that the metal Co, as the active sites in NdNi-Co$_3$O$_4$, had undergone three steps at alkaline conditions for the OER process: c-CoO$_x$→ a-CoO$_x$→a-CoOOH, and the active metal sites

on the Ni-Co$_3$O$_4$ surface were directly reconstructed from crystalline cobalt oxide to amorphous cobalt oxyhydroxide [60]. In short, the introduction of Ni into the spinel Co$_3$O$_4$ can effectively modulate the electronic structure of cobalt site and induce a significant reconstruction of the Ni-Co$_3$O$_4$ surface during the OER process. Moreover, the further introduction of Nd can transform crystalline cobalt oxide in spinel into an amorphous form, and then into amorphous hydroxyl cobalt oxide, which would promote the catalytic activity [61].

Through comparing the XRD of NdNi-Co$_3$O$_4$ catalysts before and after OER, we found no obvious change in the diffraction peaks, which indicated that there were no other new species of the spinel structure, and thus better stability of catalysts achieved (Fig. 6e). In addition, the change of elemental valency state on the catalyst surface before and after the OER was also investigated with XPS. As seen in the Co 2p spectra of Fig. 6f, the ratio of Co^{3+}/Co^{2+} increased significantly from 0.65 to1.08, while the Co^{3+} 2p binding energy decreases from 15.2 eV to 14.5 eV, indicating that the surface reconstruction of NdNi-Co$_3$O$_4$ produced a new specie cobalt oxyhydroxide [62]. Whereas, the Ni 2p spectrum showed a negligible variation (Figure S19a). In addition, as shown in Figure S19b, there is a new peak in the O 1 s at 528.6 eV, which corresponds to the O$_2^{2-}$ species, and the existence of O$_2^{2-}$ species confirmed the generation of cobalt oxyhydroxide in NdNi-Co$_3$O$_4$ after
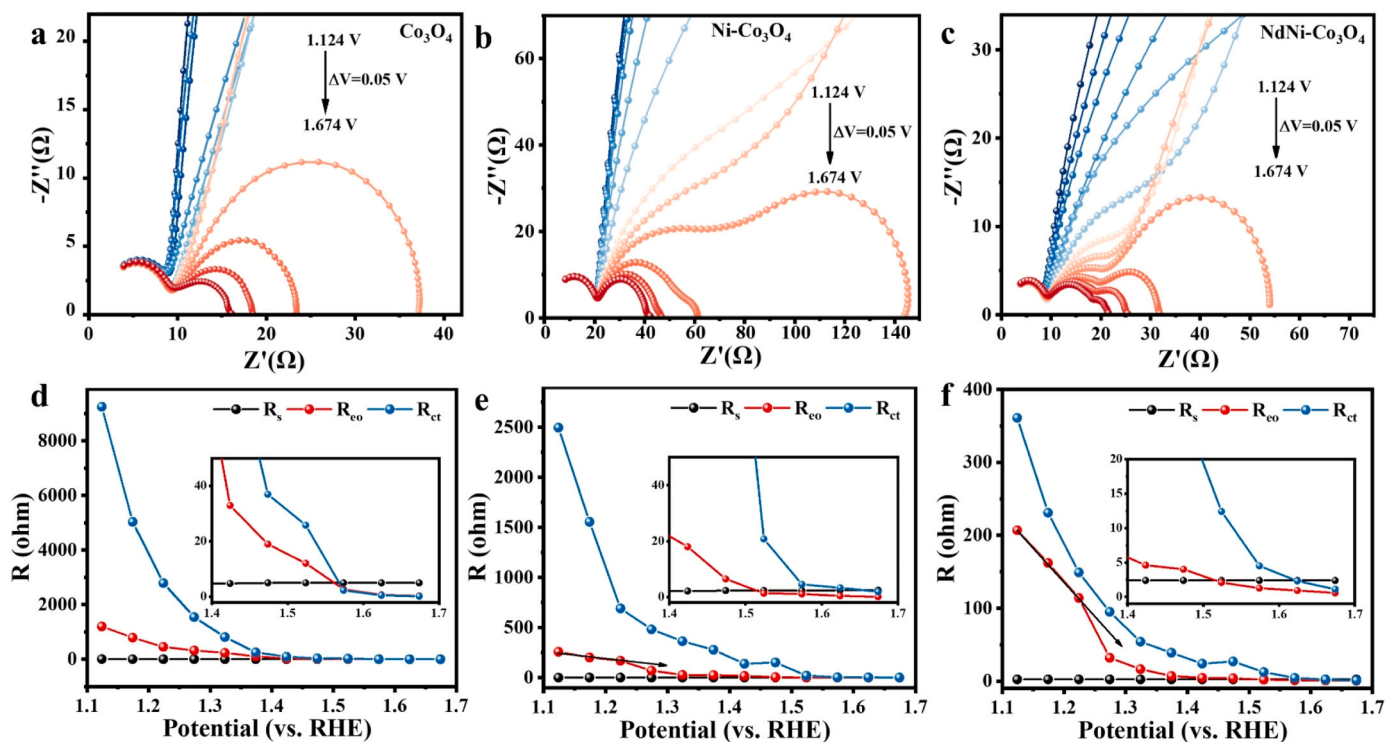
Fig. 5. (a-c) Nyquist plots, (d-f) The values of resistance obtained by DRT analysis for the catalysts at different potential in 1 M KOH.
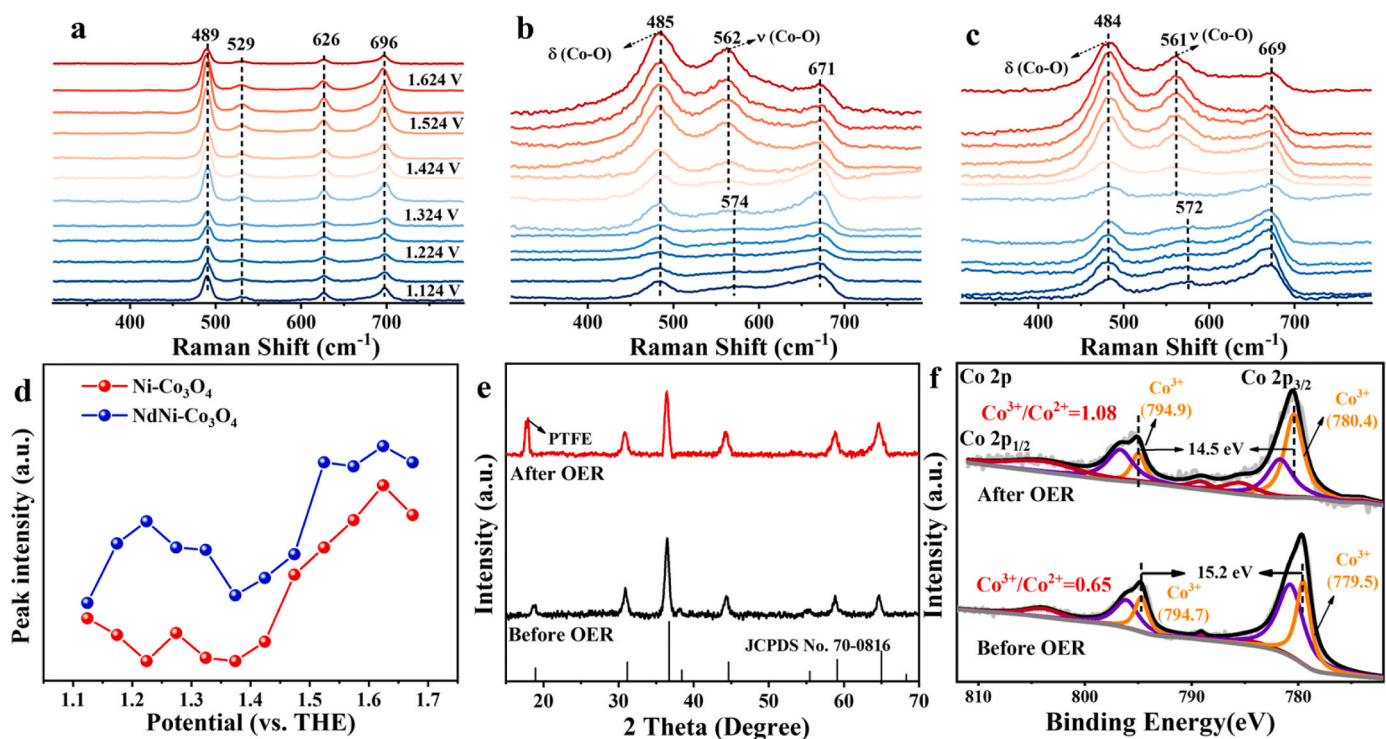

Fig. 6. In situ Raman Spectrum measurements of (a) Co_3O_4, (b) Ni-Co_3O_4 and (c) NdNi-Co_3O_4 for OER in 1 M KOH, (d) comparison of the $\nu_{(Co-O)}$ Raman peak intensity of the catalysts. (e) XRD patterns and (f) XPS spectra of Co 2p of the NdNi-Co_3O_4 before and after OER.

OER [63]. Finally, The TEM images showed that the surface of catalyst became amorphous (Figure S20). Overall, the above results validated the fact that the introduction of Ni and Nd to Co_3O_4 would facilitate the surface reconstruction in NdNi-Co_3O_4 during the OER process.

3.4. Theoretical calculations

The experimental results showed that the introduction of Ni and Nd could promote the surface reconstruction of spinel, which enhanced the OER performance of NdNi-Co_3O_4. In view of this, both the free energy of

spinel catalysts in relative to the intermediates of the OER process and the projected density of states (PDOS) were investigated through DFT calculations. The objective was to understand the mechanism of OER. Based on the structure of the catalyst, the (111) of NdNi-Co$_3$O$_4$ and the (001) of CoOOH were matched and an optimized heterostructure model for NdNi-Co$_3$O$_4$@CoOOH was proposed in Fig. 7a to simulate the real electrochemical reaction during the OER [64]. The models of CoOOH,

Co$_3$O$_4$@CoOOH and Ni-Co$_3$O$_4$@CoOOH are shown in Figure S21 of the supporting information. Also, according to the studies reported in literature, the performance of the OER is related to the energy barrier of the potential determining step (PDS) [65]. The Gibbs free energy of the four-electron OER step was calculated for CoOOH, Co$_3$O$_4$@CoOOH, Ni-Co$_3$O$_4$@CoOOH and NdNi-Co$_3$O$_4$@CoOOH, respectively, which are shown in Fig. 7b. It is obvious that the first step (the formation of *OH) is

Fig. 7. (a) Optimized initial and adsorption structures of NdNi-Co$_3$O$_4$@CoOOH for OER pathway. (b,d) Free energy for OER on the CoOOH, Co$_3$O$_4$@CoOOH, Ni-Co$_3$O$_4$@CoOOH and NdNi-Co$_3$O$_4$@CoOOH at U = 1.23 V and U = 0 V. (c,e) Comparison of the ΔG for the four steps during OER. (f) Average of the Bader charges in Table S2. (g) Projected density of states for the adsorption sites (Co atom) on catalyst surfaces.

a spontaneous process for all catalysts, which may be caused by the strong adsorption from oxygen vacancies in the spinel type oxides. However, the last two steps (the formation of *OH and O_2) require an extra energy to complete. For CoOOH and Co_3O_4@CoOOH, as shown in Fig. 7c, the fourth step had the highest free energy ($\Delta G_4 = 1.06$ and 1.60 eV), indicating the formation of O_2 was the PDS. After introducing Ni, however, the free energy of the fourth step decreased to 0.8 eV, where the formation of O_2 was still the PDS of the Ni-Co_3O_4@CoOOH. With the further introduction of Nd, the free energy of the fourth step decreased sharply to 0.37 eV, which is lower than that of the formation steps of *OOH ($\Delta G_3 = 0.47$ eV) and *OH ($\Delta G_2 = 0.40$ eV). In addition, the formation energy of *OOH had also been decreased from 0.70 eV for Ni-Co_3O_4/CoOOH to 0.47 eV for NdNi-Co_3O_4@CoOOH. In another word, the introduction of Nd not only changed PDS from O_2 formation on Ni-Co_3O_4@CoOOH to *OOH formation on NdNi-Co_3O_4@CoOOH, but also effectively decreased the energy barrier of *OOH formation. Shown in Figure S22a is the comparison of the theoretical overpotentials of the catalysts. As seen, the magnitudes follow the order of: NdNi-Co_3O_4@CoOOH < Ni-Co_3O_4@CoOOH < Co_3O_4@CoOOH. Although there are errors between the theoretical overpotential and experimental one, it is still reasonable to compare these data qualitatively [65]. The calculations for U = 0 V were also performed, which are shown in Fig. 7d, e. As seen, the catalyst NdNi-Co_3O_4@CoOOH (0.55 V) had the lowest overpotential compared to Co_3O_4@CoOOH (1.62 V) and Ni-Co_3O_4@CoOOH (0.81 V) (see Figure S22b). Furthermore, similar to U=1.23 V, the rate-limiting step of the OER process was converted from the O_2 formation to OOH* formation Therefore, it can be confirmed that the role of Ni and Nd in NdNi-Co_3O_4@CoOOH is mainly to decrease the free energy in O_2 formation, and thus converting the PDS from the O_2 formation to the *OOH formation, as well as the decrease of the energy barrier for OOH* formation in OER process. The results, observed at both U=0 and 1.23 V, showed that the introduction of Ni and Nd had changed the PDS and decreased the free energy of *OOH formation, thereby resulting in the decrease in the theoretical overpotential.

To find the relationship between the introduction of Ni & Nd and the electronic structure of the Co site, the differential charge density of the three catalysts was presented in Fig. 7f and Figure S23-24. As seen, the charge is in the order of: Co_3O_4@CoOOH (-1.44|e|) > Ni-Co_3O_4@CoOOH (-1.46|e|) > NdNi-Co_3O_4@CoOOH (-1.51|e|), which indicated that the inter-atomic electron donation is mainly from Ni and Nd to Co [66]. Moreover, the projected density of states (PDOS) further revealed the electron donation after the introduction of Ni and Nd. The overlap between the Co 3d and O 2p around the Fermi level was significantly greater in both Ni-Co_3O_4@CoOOH and NdNi-Co_3O_4@CoOOH than in Co_3O_4@CoOOH (Fig. 7g and Figure S25), indicating that an enhanced catalyst adsorption of oxygen-containing intermediate species happened during the OER process [67]. In summary, it can be concluded, from the DFT theoretical calculations, that the introduction of Ni and Nd not only effectively weakened the adsorption of the NdNi-Co_3O_4@CoOOH to the intermediates, but also promoted the oxygen formation, thus leading ultimately to the change of the PDS from O_2 formation to *OOH formation, and to the decrease of the energy barrier for *OOH formation.

4. Conclusion

In this work, a greatly improved catalyst NdNi-Co_3O_4 was prepared through introducing Ni and Nd into the spinel oxide Co_3O_4, which exhibited a lowest overpotential (269 mV) at 10 mA·cm^{-2}, compared to the other catalysts such as Ni-Co_3O_4 (305 mV) and Co_3O_4 (393 mV). Additionally, the generation and dynamic change of the active species on the catalyst surface were monitored via both in-situ Raman and in-situ impedance to gain the insight into the effect of the introduced Ni and Nd on the surface reconstruction of Co-based spinel oxides during the OER process. It was found that the NdNi-Co_3O_4 exhibited a dynamic reconstruction process when the potential was increased; in addition, the resistance of catalyst electrooxidation was decreased due to the Ni-

substitution, which could facilitate the generation of CoOOH. At the same time, the Nd-substitution resulted in the conversion of crystalline cobalt oxide into amorphous CoO_x, which ultimately led to the formation of CoOOH at the low overpotential. In other words, the metal active sites on the surface of NdNi-Co_3O_4 spinel oxide at low overpotential underwent a completely different three-steps reconstruction process: crystalline CoO_x → amorphous CoO_x → amorphous CoOOH, in comparison with Co_3O_4 and Ni-Co_3O_4. Moreover, the theoretical calculations showed that the co-doping of Ni and Nd in spinel oxides would change the PDS from O_2 formation to the *O → *OOH formation, as it had a decreased energy barrier in the formation of *OOH. In summary, this work provided an insightful understanding to the effect of tetrahedral and octahedral site modulation in spinel oxides on surface reconstruction during the OER process, which might offer an effective pathway for the proper and accurate design of efficient OER electrocatalysts when transition metal oxides were employed.

CRediT authorship contribution statement

Zhijin Wang: Resources, Investigation, Data curation. **Tao Li:** Writing – original draft, Investigation, Formal analysis, Data curation, Conceptualization. **Yun-Quan Liu:** Writing – review & editing, Supervision, Project administration, Formal analysis, Conceptualization. **Mingyu Wang:** Resources. **Linhai Wang:** Resources, Methodology.

Declaration of Competing Interest

The authors declare that they have no known competing financial interests or personal relationships that could have appeared to influence the work reported in this paper.

Data availability

Data will be made available upon request.

Acknowledgement

Appendix A. Supporting information

Supplementary data associated with this article can be found in the online version at doi:10.1016/j.apcatb.2024.123990.

References

[1] S.Z. Oener, M.J. Foster, S.W. Boettcher, Accelerating water dissociation in bipolar membranes and for electrocatalysis, Science 369 (2020) 1099–1103.

[2] Y. Rao, S. Chen, Q. Yue, Y. Kang, Optimizing the spin states of mesoporous Co_3O_4 nanorods through vanadium doping for long-lasting and flexible rechargeable Zn-air batteries, ACS Catal. 11 (2021) 8097–8103.

[3] C. Zhao, J. Liu, J. Wang, C. Wang, X. Guo, X. Li, X. Chen, L. Song, B. Li, Q. Zhang, A clicking confinement strategy to fabricate transition metal single-atom sites for bifunctional oxygen electrocatalysis, Sci. Adv. 8 (2022) abn5091.

[4] Z. Huang, J. Song, Y. Du, S. Xi, S. Dou, J.M.V. Nsanzimana, C. Wang, Z.J. Xu, X. Wang, Chemical and structural origin of lattice oxygen oxidation in Co-Zn oxyhydroxide oxygen evolution electrocatalysts, Nat. Energy 4 (2019) 329–338.

[5] Z. Yu, C. Si, A.P. LaGrow, Z. Tai, W.A. Caliebe, A. Tayal, M.J. Sampaio, J.P. S. Sousa, I. Amorim, A. Araujo, L. Meng, J.L. Faria, J. Xu, B. Li, L. Liu, Iridium-iron diatomic active sites for efficient bifunctional oxygen electrocatalysis, ACS Catal. 12 (2022) 9397–9409.

[6] J. Wang, C. Cheng, Q. Yuan, H. Yang, F. Meng, Q. Zhang, L. Gu, J. Cao, L. Li, S. Haw, Q. Shao, L. Zhang, T. Cheng, F. Jiao, X. Huang, Exceptionally active and stable RuO_2 with interstitial carbon for water oxidation in acid, Chem 8 (2022) 1673–1687.

[7] C. Deng, C.Y. Toe, X. Li, J. Tan, H. Yang, Q. Hu, C. He, Earth-abundant metal-based electrocatalysts promoted anodic reaction in hybrid water electrolysis for efficient hydrogen production: recent progress and perspectives, Adv. Energy Mater. 12 (2022) 2201047.

[8] H. Yang, Y. Liu, S. Luo, Z. Zhao, X. Wang, Y. Luo, Z. Wang, J. Jin, J. Ma, Lateral-Size-mediated efficient oxygen evolution reaction: insights into the atomically thin quantum dot structure of NiFe$_2$O$_4$, ACS Catal. 7 (2017) 5557–5567.

[9] Y. Zhou, S. Xu, J. Wang, S. Sun, C. Wei, Z. Feng, Y. Du, Z.J. Xu, Revealing the dominant chemistry for oxygen reduction reaction on small oxide nanoparticles, ACS Catal. 8 (2018) 673–677.

[10] J.O. Olowoyo, R.J. Kriek, Recent progress on bimetallic-based spinels as electrocatalysts for the oxygen evolution reaction, Small 18 (2022) 2106187.

[11] W. Guo, H. Luo, D. Fang, Z. Jiang, J. Chi, W. Shangguan, *In situ* revealing the reconstruction behavior of monolayer rocksalt CoO nanosheet as water oxidation catalyst, J. Energy Chem. 70 (2022) 373–381.

[12] K. Xiao, Y. Wang, P. Wu, L. Hou, Z.-Q. Liu, Activating lattice oxygen in spinel ZnCo$_2$O$_4$ through filling oxygen vacancies with fluorine for electrocatalytic oxygen evolution, Angew. Chem. Int. Ed. 62 (2023) e202301408.

[13] Z. Zeng, S. Kuang, Z. Huang, X. Chen, Y. Su, Y. Wang, S. Zhang, X. Ma, Boosting oxygen evolution over inverse spinel Fe-Co-Mn oxide nanocubes through electronic structure engineering, Chem. Eng. J. 433 (2022) 134446.

[14] Z. Liu, G. Wang, X. Zhu, Y. Wang, Y. Zou, S. Zang, S. Wang, Optimal geometrical configuration of cobalt cations in spinel oxides to promote oxygen evolution reaction, Angew. Chem. Int. Ed. 59 (2020) 4736–4742.

[15] C. Fan, X. Wu, M. Li, X. Wang, Y. Zhu, G. Fu, T. Ma, Y. Tang, Surface chemical reconstruction of hierarchical hollow inverse-spinel manganese cobalt oxide boosting oxygen evolution reaction, Chem. Eng. J. 431 (2022) 133829.

[16] D. Guan, C. Shi, H. Xu, Y. Gu, J. Zhong, Y. Sha, Z. Hu, M. Ni, Z. Shao, Simultaneously mastering operando strain and reconstruction effects via phase-segregation strategy for enhanced oxygen-evolving electrocatalysis, J. Energy Chem. 82 (2023) 572–580.

[17] F. Yu, S. Bo, X. Zhang, H. Su, M. Liu, W. Zhou, X. Sun, Y. Xu, H. Zhang, F. Yu, W. Wang, Q. Liu, Valence-modified selenospinels as ampere-current-bearing oxygen evolution catalysts, Appl. Catal. B-Environ. Energy 316 (2022) 121649.

[18] Y. Sun, J. Wu, Y. Xie, K. Wang, K. Ma, Z. Tian, Z. Zhang, Q. Liao, W. Zheng, Z. Kang, Y. Zhang, Dynamics of both active phase and catalysis pathway for spinel water-oxidation catalysts, Adv. Funct. Mater. 32 (2022) 2207116.

[19] Y. Peng, C. Huang, J. Huang, M. Feng, X. Qiu, X. Yue, S. Huang, Filling octahedral interstices by building geometrical defects to construct active sites for boosting the oxygen evolution reaction on NiFe$_2$O$_4$, Adv. Funct. Mater. 32 (2022) 2201011.

[20] H. Xu, J. Yuan, G. He, H. Chen, Current and future trends for spinel-type electrocatalysts in electrocatalytic oxygen evolution reaction, Coordi. Chem. Rev. 475 (2023) 214869.

[21] Z. Wang, J. Huang, L. Wang, Y. Liu, W. Liu, S. Zhao, Z. Liu, Cation-tuning induced d-band center modulation on co-based spinel oxide for oxygen reduction/evolution reaction, Angew. Chem. Int. Ed. 61 (2022) e202114696.

[22] H. Wang, S. Hung, H. Chen, T. Chan, H.M. Chen, B. Liu, In-operando identification of geometrical-site-dependent water oxidation activity of spinel Co$_3$O$_4$, J. Am. Chem. Soc. 251 (2016) 36–39.

[23] S. Sun, Y. Sun, Y. Zhou, J. Shen, D. Mandler, R. Neumann, Z.J. Xu, Switch of the rate-determining step of water oxidation by spin-selected electron transfer in spinel oxides, Chem. Mater. 31 (2019) 8106–8111.

[24] Z. Huang, X. Liao, W. Zhang, J. Hu, Q. Gao, Ceria-promoted reconstruction of Ni-based electrocatalysts toward efficient oxygen evolution, ACS Catal. 12 (2022) 13951–13960.

[25] Z. Chen, H. Yang, Z. Kang, M. Driess, P.W. Menezes, The pivotal role of s-, p-, and f-block metals in water electrolysis: status quo and perspectives, Adv. Mater. 34 (2022) e2108432.

[26] J. Qian, X. Liu, C. Zhong, G. Xu, H. Li, W. Zhou, B. You, F. Wang, D. Gao, D. Chao, Enhanced stability and narrowed D-band gap of Ce-doped Co$_3$O$_4$ for rechargeable aqueous Zn-air battery, Adv. Funct. Mater. 33 (2023) 2207116.

[27] J. Yang, Y. Wang, J. Yang, Y. Pang, X. Zhu, Y. Lu, Y. Wu, J. Wang, H. Chen, Z. Kou, Z. Shen, Z. Pan, J. Wang, Quench-induced surface engineering boosts alkaline freshwater and seawater oxygen reaction of porous NiCo$_2$O$_4$ nanowires, Small 18 (2022) 2106187.

[28] N.C. Maile, M. Moztahida, A.A. Ghani, M. Hussain, K. Tahir, B. Kim, S.K. Shinde, V. J. Fulari, D.S. Lee, Electrochemical synthesis of binder-free interconnected nanosheets of Mn-doped Co$_3$O$_4$ on Ni foam for high-performance electrochemical energy storage application, Chem. Eng. J. 421 (2021) 129767.

[29] R. Zhang, L. Pan, B. Guo, Z. Huang, Z. Chen, L. Wang, X. Zhang, Z. Guo, W. Xu, K. P. Loh, J. Zou, Tracking the role of defect types in Co$_3$O$_4$ structural evolution and active motifs during oxygen evolution reaction, J. Am. Chem. Soc. 145 (2023) 2271–2281.

[30] J. Liu, M. Zheng, J. Li, Y. Yuan, C. Li, S. Zhang, L. Yang, Z. Bai, J. Lu, Lithiation-induced defect engineering to promote oxygen evolution reaction, Adv. Funct. Mater. 33 (2023) 2209753.

[31] X. Gao, X. Liu, S. Wang, W. Zhang, H. Lin, R. Cao, Black phosphorus incorporated cobalt oxide: biomimetic channels for electrocatalytic water oxidation, Chin. J. Catal. 43 (2022) 1123–1130.

[32] F. Tang, S. Guo, Y. Sun, X. Lin, J. Qiu, A. Cao, Facile synthesis of Fe-doped CoO nanotubes as high-efficient electrocatalysts for oxygen evolution reaction, Small Struct. 3 (2022) 2100211.

[33] V. Bilovol, S. Ferrari, D. Derewnicka, F.D. Saccone, XANES and XPS study of electronic structure of Ti-enriched Nd-Fe-B ribbons, Mater. Chem. Phys. 146 (2014) 269–276.

[34] C. Chen, H. Su, L. Lu, Y. Hong, Y. Chen, K. Xiao, T. Ouyang, Y. Qin, Z. Liu, Interfacing spinel NiCo$_2$O$_4$ and NiCo alloy derived N-doped carbon nanotubes for enhanced oxygen electrocatalysis, Chem. Eng. J. 408 (2021) 127814.

[35] Y. Liu, Y. Chen, X. Mu, Z. Wu, X. Jin, J. Li, Y. Xu, L. Yang, X. Xi, H. Jang, Z. Lei, Q. Liu, S. Jiao, P. Yan, X. Li, R. Cao, Spinel-anchored iridium single atoms enable efficient acidic water oxidation via intermediate stabilization effect, ACS Catal. 13 (2023) 3757–3767.

[36] B. He, G. Pan, Y. Deng, L. Zhao, H. Wang, R. Wang, Y. Gong, Hierarchical iron-phosphide@NiCo$_2$O$_4$ nanoneedle arrays for high performance water splitting, Appl. Surf. Sci. 569 (2021) 151016.

[37] X. Wang, Y. Zhou, J. Luo, F. Sun, J. Zhang, Synthesis of V-doped urchin-like NiCo$_2$O$_4$ with rich oxygen vacancies for electrocatalytic oxygen evolution reactions, Electrochim. Acta 406 (2022) 139800.

[38] X. Zhai, H. Pan, F. Wang, X. Gao, Z. Xiong, L. Li, Q. Chang, S. Cheng, Z. Zuo, Y. Li, Controlled growth of 3D interpenetrated networks by NiCo$_2$O$_4$ and graphdiyne for high-performance supercapacitor, ACS Appl. Mater. Interfaces 14 (2022) 18283–18292.

[39] C. Cheng, L. Mao, J. Shi, F. Xue, S. Zong, B. Zheng, L. Guo, NiCo$_2$O$_4$ nanosheets as a novel oxygen-evolution-reaction cocatalyst *in situ* bonded on the g-C$_3$N$_4$ photocatalyst for excellent overall water splitting, J. Mater. Chem. A 9 (2021) 12299–12306.

[40] W. Deeloed, T. Priamushko, J. Cizek, S. Suramitr, F. Kleitz, Defect-engineered hydroxylated mesoporous spinel oxides as bifunctional electrocatalysts for oxygen reduction and evolution reactions, ACS Appl. Mater. Interfaces 14 (2022) 23307–23321.

[41] X. Zhang, F. Yan, X. Ma, C. Zhu, Y. Wang, Y. Xie, S. Chou, Y. Huang, Y. Chen, Regulation of morphology and electronic structure of FeCoNi layered double hydroxides for highly active and stable water oxidization catalysts, Adv. Energy Mater. 11 (2021) 2102141.

[42] P. Zhou, X. Lv, S. Tao, J. Wu, H. Wang, X. Wei, T. Wang, B. Zhou, Y. Lu, T. Frauenheim, X. Fu, S. Wang, Y. Zou, Heterogeneous-interface-enhanced adsorption of organic and hydroxyl for biomass electrooxidation, Adv. Mater. 34 (2022) e2204089.

[43] Z. Xiao, Y. Huang, C. Dong, C. Xie, Z. Liu, S. Du, W. Chen, D. Yan, L. Tao, Z. Shu, G. Zhang, H. Duan, Y. Wang, Y. Zou, R. Chen, S. Wang, Operando identification of the dynamic behavior of oxygen vacancy-rich Co$_3$O$_4$ for oxygen evolution reaction, J. Am. Chem. Soc. 142 (2020) 12087–12095.

[44] W. Chen, L. Xu, X. Zhu, Y. Huang, W. Zhou, D. Wang, Y. Zhou, S. Du, Q. Li, C. Xie, L. Tao, C. Dong, J. Liu, Y. Wang, R. Chen, H. Su, C. Chen, Y. Zou, Y. Li, Q. Liu, S. Wang, Unveiling the electrooxidation of urea: intramolecular coupling of the N-N bond, Angew. Chem. Int. Ed. 60 (2021) 7297–7307.

[45] S. Fu, Y. Ma, X. Yang, X. Yao, Z. Jiao, L. Cheng, P. Zhao, Defect and interface engineering of hexagonal Fe$_2$O$_3$/ZnCo$_2$O$_4$ n-n heterojunction for efficient oxygen evolution reaction, Appl. Catal. B Environ. 333 (2023) 122813.

[46] L. Ji, J. Wang, X. Teng, T.J. Meyer, Z. Chen, CoP nanoframes as bifunctional electrocatalysts for efficient overall water splitting, ACS Catal. 10 (2020) 412–419.

[47] X. Chen, Q. Wang, Y. Cheng, H. Xing, J. Li, X. Zhu, L. Ma, Y. Li, D. Liu, S-doping triggers redox reactivities of both iron and lattice oxygen in FeOOH for low-cost and high-performance water oxidation, Adv. Funct. Mater. 32 (2022) 2112674.

[48] Z. Zhan, X. Liang, J. Li, J. Qian, Y. Liu, S. Yang, Y. Wang, D. Gao, D. Xue, Interfacial engineering of NiO/NiCo$_2$O$_4$ porous nanofibers as efficient bifunctional catalysts for rechargeable zinc-air batteries, ACS Appl. Mater. Interfaces 12 (2020) 21661–21669.

[49] S. Liu, B. Zhang, Y. Cao, H. Wang, Y. Zhang, S. Zhang, Y. Li, H. Gong, S. Liu, Z. Yang, J. Sun, Understanding the effect of nickel doping in cobalt spinel oxides on regulating spin state to promote the performance of the oxygen reduction reaction and zinc-air batteries, ACS Energy Lett. 8 (2022) 159–168.

[50] W. Tang, J. Tang, K. Liao, Z. Shao, Self-reconstruction of highly active NiCo$_2$O$_4$ with triple-continuous transfer of electrons, ions, and oxygen for Zn-air batteries, Chem. Eng. J. 455 (2023) 140855.

[51] J. Bejar, L. Alvarez Contreras, J. Ledesma-Garcia, N. Arjona, L.Gerardo Arriaga, An advanced three-dimensionally ordered macroporous NiCo$_2$O$_4$ spinel as a bifunctional electrocatalyst for rechargeable Zn-air batteries, J. Mater. Chem. A 8 (2020) 8554–8565.

[52] K. Zeng, W. Li, Y. Zhou, Z. Sun, C. Lu, J. Yan, J. Choi, R. Yang, Multilayer hollow MnCo$_2$O$_4$ microsphere with oxygen vacancies as efficient electrocatalyst for oxygen evolution reaction, Chem. Eng. J. 421 (2021) 126400.

[53] Z. Zhang, J. Li, J. Qian, Z. Li, L. Jia, D. Gao, D. Xue, Significant change of metal cations in geometric sites by magnetic-field annealing FeCo$_2$O$_4$ for enhanced oxygen catalytic activity, Small 18 (2022) 2104248.

[54] J. Zhang, J. Li, C. Zhong, P. Xi, D. Chao, D. Gao, Surface-electronic-structure reconstruction of perovskite via double-cation gradient etching for superior water oxidation, Nano Lett. 21 (2021) 8166–8174.

[55] B. Qiu, C. Wang, N. Zhang, L. Cai, Y. Xiong, Y. Chai, CeO$_2$-induced interfacial Co^{2+} octahedral sites and oxygen vacancies for water oxidation, ACS Catal. 9 (2019) 6484–6490.

[56] J. Choi, D. Kim, S.J. Hong, X. Zhang, H. Hong, H. Chun, B. Han, L.Y.S. Lee, Y. Piao, Tuning the electronic structure and inverse degree of inverse spinel ferrites by integrating samarium orthoferrite for efficient water oxidation, Appl. Catal. B Environ. 315 (2022) 121504.

[57] W. Tang, K. Teng, W. Guo, F. Gu, B. Li, R. Qi, R. Liu, Y. Lin, M. Wu, Y. Chen, Defect-engineered Co$_3$O$_4$@nitrogen-deficient graphitic carbon nitride as an efficient bifunctional electrocatalyst for high-performance metal-air batteries, Small 18 (2022) 2202194.

[58] X. Li, L. Zhang, Q. Deng, S. Chen, J. Wang, Z. Zeng, S. Deng, Promoted hydrogenolysis of furan aldehydes to 2,5-dimethylfuran by defect engineering on Pd/NiCo$_2$O$_4$, Chemsuschem 15 (2022) e202102532.

[59] T. Wu, S. Sun, J. Song, S. Xi, Y. Du, B. Chen, W.A. Sasangka, H. Liao, C.L. Gan, G. G. Scherer, L. Zeng, H. Wang, H. Li, A. Grimaud, Z.J. Xu, Iron-facilitated dynamic active-site generation on spinel CoAl$_2$O$_4$ with self-termination of surface reconstruction for water oxidation, Nat. Catal. 2 (2019) 763–772.

[60] Y. Liu, Z. Chen, Z. Li, N. Zhao, Y. Xie, Y. Du, J. Xuan, D. Xiong, J. Zhou, L. Cai, Y. Yang, CoNi nanoalloy-Co-N$_4$ composite active sites embedded in hierarchical porous carbon as bi-functional catalysts for flexible Zn-air battery, Nano Energy 99 (2022) 107325.

[61] Y. Wang, Z. Wang, H. Wu, L. Hou, Z. Liu, Reconstruction of spinel Co$_3$O$_4$ by inert Zn^{2+} towards enhanced oxygen catalytic activity, Chem. Commun. 58 (2022) 637–640.

[62] L. An, H. Zhang, J. Zhu, S. Xi, B. Huang, M. Sun, Y. Peng, P. Xi, C.-H. Yan, Balancing activity and stability in spinel cobalt oxides through geometrical sites occupation towards efficient electrocatalytic oxygen evolution, Angew. Chem. Int. Ed. 62 (2023) e202214600.

[63] D. Liu, H. Ai, J. Li, M. Fang, M. Chen, D. Liu, X. Du, P. Zhou, F. Li, K.H. Lo, Y. Tang, S. Chen, L. Wang, G. Xing, H. Pan, Surface reconstruction and phase transition on vanadium-cobalt-iron trimetal nitrides to form active oxyhydroxide for enhanced electrocatalytic water oxidation, Adv. Energy Mater. 10 (2020) 2002464.

[64] L. Yang, H. Qin, Z. Dong, T. Wang, G. Wang, L. Jiao, Metallic S-CoTe with surface reconstruction activated by electrochemical oxidation for oxygen evolution catalysis, Small 17 (2021) 2102027.

[65] N.C.S. Selvam, S.J. Kwak, G.H. Choi, M.J. Oh, H. Kim, W.-S. Yoon, W.B. Lee, P. J. Yoo, Unveiling the impact of Fe incorporation on intrinsic performance of reconstructed water oxidation electrocatalyst, ACS Energy Lett. 6 (2021) 4345–4354.

[66] A. Yang, K. Su, W. Lei, Y. Tang, X. Qiu, Ternary synergism of heterogeneous M^{1}N$_4$-M^{2}N$_4$-C-M^{3}N$_4$ single-atom sites to manipulate the electrocatalytic pathway for Zn-air battery and water splitting, Adv. Energy Mater. 13 (2023) 2203150.

[67] W. Huang, J. Li, X. Liao, R. Lu, C. Ling, X. Liu, J. Meng, L. Qu, M. Lin, X. Hong, X. Zhou, S. Liu, Y. Zhao, L. Zhou, L. Mai, Ligand modulation of active sites to promote electrocatalytic oxygen evolution, Adv. Mater. 34 (2022) e2200270.